A CONTROL THEORY APPROACH TO ADAPTIVE STEPSIZE SELECTION FOR COUPLED CFD AND CRUD CHEMISTRY SIMULATIONS

Daniel Walter, Victor Petrov, and Annalisa Manera
Department of Nuclear Engineering and Radiological Sciences, University of Michigan,
2355 Bonisteel Boulevard, Ann Arbor, 48109-2104 Michigan, USA
djwalter@umich.edu; petrov@umich.edu; manera@umich.edu

Brian K. Kendrick
Theoretical Division (T-1, MS B221), Los Alamos National Laboratory
Los Alamos, New Mexico 87545, USA
bkendric@lanl.edu

ABSTRACT

A control theory approach is adopted to determine the temporal discretization of exchanging data during coupled computational fluid dynamics (CFD) and CRUD chemistry/deposition simulations. The benefit of automated and adaptive stepsize control is realized in high-fidelity multiphysics simulations where the physics are nonlinear in time and stepsize changes may be necessary to ensure a converged coupled solution is obtained. A conventional predictor-corrector method is used to address the nonlinearity of the coupled problem, including the feedbacks between the cladding temperature, heat flux, CRUD deposition, and boron precipitation. The strong time-dependency of the boron precipitation is the motivation for seeking an adaptive stepsize method. The predictor and corrector solutions obtained are used to approximate the residual of the nonlinear solution. A user-specified tolerance on the change in the boron mass is set to control the convergence residual of the coupled solution. A proportional-integral controller is parameterized and applied to control the temporal data exchange between CRUD deposition and CFD solutions during a 500-day cycle simulation. A single three-dimensional fuel pin cell with three spacer grids with mixing vanes is used in this study.

KEYWORDS
adaptive stepsize, multiphysics, CRUD, coupled CFD, control theory

1. INTRODUCTION

1.1. Background

Modeling the individual physics within a nuclear reactor has been an active area of research for half a century. In the last decade, the paradigm has shifted to multiphysics simulations where coupling of the (historically) separate physics is performed to improve predictions. Loose coupling refers to exchanging data between multiple physics and uses fixed-point iteration (FPI) and/or predictor-corrector (P-C) type methods to converge the solution. Tight coupling refers to a monolithic formulation and solution of the coupled equations. The work in this paper is aimed at optimizing the temporal discretization of the data exchange between loosely coupled physics. Specifically, the high-fidelity simulation of CRUD (Chalk River Unidentified Deposit), or corrosion particulate, deposition on the surface of pressurized water reactor (PWR) fuel rods is under investigation. Previous works have introduced the multiphysics

framework where the coupling of neutron transport, computational fluid dynamics (CFD), and CRUD chemistry is developed [1,2]; initial validation with plant data has also been completed [3]. Additionally, other efforts using industry-standard tools have investigated this multiphysics problem—the coupling of ANC, VIPRE, and BOA [4,5]. The coupling between VIPRE and ANC featured a two-way data exchange interface, which used FPI to converge the nonlinear solution. The three way coupling with BOA was completed by a one-way data transfer from VIPRE to BOA and another from BOA to ANC. A time-consistent solution was eventually obtained by embedding the FPI within a predictor-corrector method.

Because the coupled physics of neutron transport, nuclide depletion, hydraulics, heat transfer, coolant chemistry, and CRUD deposition are highly nonlinear, a systematic investigation of the feedback mechanisms and solution sensitivities to the coupled time stepsize is necessary. Particularly, the temporal coupling of steady state thermal hydraulics, via CFD and time-dependent CRUD deposition is investigated for a 500-day operating cycle. First, the 500-day cycle simulation is discretized using several fixed time stepsizes, including 50, 25, and 5 days. For each of the fixed stepsize simulations, three additional coupled CFD and CRUD chemistry cases are considered:

1. one-way explicit (time-lagged) coupling, where CFD provides the thermal hydraulic boundary conditions to the CRUD deposition simulation without feedback,
2. two-way explicit (time-lagged) coupling, where the CFD and CRUD data are exchanged at the beginning of each time step, where feedback through the thermal hydraulics is included,
3. and, a two-way predictor-corrector (time-consistent) coupling, where two CFD and CRUD simulations are run per time step; the step-average of the thermal hydraulic properties is used in the second CRUD deposition simulation.

Second, an adaptive stepsize selection algorithm is introduced and applied to the coupled cycle simulation. The algorithm is based on control theory and utilizes the predictor and corrector solutions to approximate the convergence residual of the coupled CFD and CRUD deposition solutions for a given time step. The boron mass within the CRUD deposit, as predicted by the CRUD deposition physics solver, is used as the *control variable* to predict the next time stepsize.

In addition to the lagged and standard predictor-corrector approaches, three other relevant temporal coupling schemes are acknowledged but have not yet been investigated in this work: (i) using an average (or middle) step value of the CRUD solution to calculate the end of step thermal hydraulic state, (ii) using a P-C method with a linear interpolation of the thermal hydraulic state to be used in the corrector calculation of the CRUD solution, (iii) and, iterating the two physics until convergence at each time step.

1.2. A Coupled Approach

In this section, simplified forms of the coupled equations are presented to expose the coupling variables. Because the high-fidelity prediction of CRUD deposition involves several complex and coupled solution methods, a useful form to express the coupled equations is through the use of a specific physics operator that transforms its inputs into outputs. The physics of lattice depletion is neglected from this discussion because the focus of this paper is on coupled CFD and CRUD deposition simulations; however, the feedbacks between the lattice depletion and CRUD deposition physics are important and should be further investigated. Figure 1 illustrates the boundary conditions that are exchanged between the CFD and CRUD deposition physics solvers.

The CFD with conjugate heat transfer (CHT) physics is represented by two operators: $\mathbb{F}$ for the fluid-flow and $\mathbb{H}_s$ for the heat transfer. The coupled input to the fluid-dynamics solver includes the cladding heat flux q'', and the outputs are the coolant temperature T_{cool}, coolant density ρ_{cool}, and turbulent kinetic energy near the cladding wall TKE:

$$(T_{cool}, \rho_{cool}, TKE) = \mathbb{F}(q''). \quad (1)$$

The inputs to the (CFD) heat transfer solver include the volumetric heat generation rate Q''' within the fuel, the coolant temperature, and the CRUD thermal resistance. The outputs are the fuel temperature, cladding temperature, and cladding heat flux:

$$\left(T_{fuel}, T_{clad}, q''\right) = \mathbb{H}_s(Q''', T_{cool}, R_c). \quad (2)$$

The CRUD chemistry operator $\mathbb{C}$ takes the inputs from the CFD operators and returns the CRUD thickness and thermal resistance:

$$(\delta_c, R_c) = \mathbb{C}(T_{clad}, q'', T_{cool}, TKE). \quad (3)$$

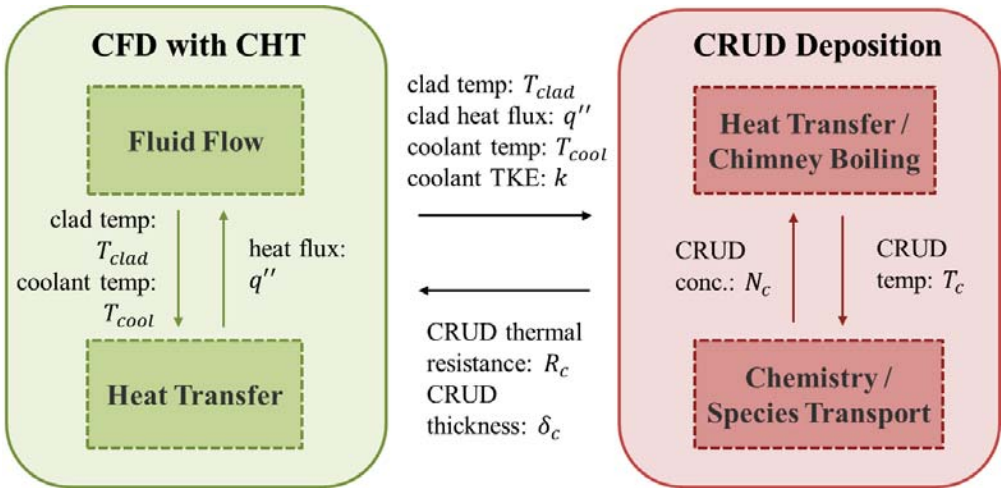

Figure 1. Boundary condition coupling between the physics of CFD and CRUD deposition.

The STAR-CCM+ [6] and MAMBA [7] codes are used for the CFD and CRUD deposition solvers, respectively. The 3-D whole-core transport code DeCART [8] is used to provide the intra-pin power density distribution to STAR-CCM+ at each time step.

2. THEORY

2.1. CRUD Deposition Physics

Species i that are modeled within MAMBA and are available to deposit within the CRUD layer include nickel ferrite ($NiFe_2O_4$), nickel oxide (NiO), iron oxide (Fe_3O_4), lithium tetraborate ($Li_2B_4O_7$), lithium monoborate ($LiBO_2$), bonnacordite (Ni_2FeBO_5), and metaboric acid (HBO_2).

The precipitation of various solid phase compounds is governed by equilibrium thermodynamics and is a function of the compound concentration and temperature. The temperature dependence of the equilibrium constants, K, are typically fit to experimental data using a three-term correlation of the general form

$$\log K_i = A + \frac{B}{T} + C \log T, \quad (4)$$

where A, B, and C are fitting constant [9]. Ref. 9 details the development of a solubility correlation for lithium monoborate, which is implemented within MAMBA with coefficients of $A = -11.19885$,

$B = 2531.638$, and $C = 5.1128$. Similar proprietary correlations are implemented for lithium tetraborate and bonnacordite. The lithium tetraborate precipitation reaction is given by

$$2Li^+ + 4B(OH)_3 \rightarrow Li_2B_4O_7 + 5H_2O + 2H^+. \quad (5)$$

Because lithium tetraborate is the least soluble and precipitates out of solution first (in comparison to the other boron-containing compounds of interest), this particular compound is the dominating *solid* boron phase within the CRUD layer modeled by MAMBA. The dominant *soluble* boron species is metaboric acid, which is added to the coolant within pressurized water reactors to control reactivity. The combination of the presence of lithium tetraborate and metaboric acid within CRUD deposits is believed to be the strongest contributor to CRUD-induced power shift (CIPS).

The presence of solid boron phases also impacts the CRUD-induced localized corrosion (CILC) condition of the plant due to changes in the specific heat capacity and thermal conductivity of the CRUD layer. In general, the introduction of solid boron phases within the porous CRUD structure increases the thermal resistance, and temperature, of the corrosion deposit. This behavior is attributed to less convective cooling because the porous CRUD layer, including *chimneys,* are filled by the solid boron phases, thus restricting the flowing water's ability to remove heat. However, there is a tradeoff between convective and conductive heat transfer as boron phases fill the CRUD pores. The thermal conductivity of the water present in the porous structure is lower than that of the solid CRUD/boron mixture, so heat conduction will be more efficient as the CRUD layer densifies.

The effective thermal conductivity of the CRUD is calculated as a standard mixing fraction where the conductivity of water, k_w, and of CRUD, k_c, are weighted by the CRUD porosity,

$$k(\vec{r}, T) = \eta(\vec{r})k_w(T) + \big(1 - \eta(\vec{r})\big)k_c. \quad (6)$$

The solid CRUD's thermal conductivity is fixed at $1.1\, W/(m \cdot K)$, which was determined based on experimental CRUD growth studies at the WALT Loop [10]. Moreover, the CRUD chimney property values were previously optimized by fitting the MAMBA-computed CRUD temperature to the WALT Loop data. These properties include a chimney radius of $4\, \mu m$, surface density ρ_{chim} of $1.6x10^5\ cm^{-2}$, and heat transfer coefficient H of $2.12x10^6\ W/(m^2 \cdot K)$.

Similar to the effective thermal conductivity, the specific heat capacity c_v is also weighted by the CRUD porosity as,

$$c_v(\vec{r}, T) = \eta(\vec{r})\rho_w(T)c_v^w(T) + \big(1 - \eta(\vec{r})\big)\rho_c c_v^c(T), \quad (7)$$

where the bulk density of the CRUD ρ_c is fixed at $5.33\ g/cm^3$. The water properties are a function of pressure and temperature; NIST correlations are utilized. For reference, the thermal conductivity at standard operating temperature and pressure is approximately $0.6\ W/(m \cdot K)$. Whereas, the specific heat capacity of the solid CRUD c_v^c, composed primarily of nickel ferrite (a.k.a. trevorite), is calculated as a function of temperature from a correlation developed in Ref. 11.

The time-dependent CRUD porosity η for species i is initialized as 0.7 and is calculated during the cycle simulation as

$$\rho_c \frac{d\eta(\vec{r})}{dt} = -N_i^c m_i, \quad (8)$$

where the mass m of species i is calculated as the product of the molecular mass M_i, concentration N_i, and volume V_i. The chimney boiling model is a modified Cohen-type model [12,13], where the boiling heat flux leaving a given CRUD volume element is expressed as

$$q_b'' = H\rho_{chim}A_{chim}\kappa(\eta)(T - T_{sat}). \tag{9}$$

The effective bulk chimney heat transfer coefficient is H, the effective bulk chimney boiling surface area is given by A_{chim}; the porosity-dependent CRUD permeability is κ; T is the local CRUD temperature; and, T_{sat} is the local liquid saturation temperature, which is a function of the local soluble boric acid concentration. If the CRUD temperature is less than the saturation temperature then the boiling heat flux is set to zero. The boiling heat flux acts as a localized "sink" in the heat transport calculation, thus resulting in a decreased thermal resistance across the CRUD deposit. This boiling model has been benchmarked against the models used in BOA [14] and successfully validated against WALT Loop experiments [10,15].

3.2. Temporal Stepsize Control

In this section, relevant aspects of control theory and its application to numerical stepsize control is briefly introduced. The works of Söderlind and Gustafsson makeup the majority of the literature on control theory applications to automate stepsize control of numerical integration methods. Gustafsson, Lundh, and Soderlind originally viewed the stepsize selection in the numerical solution of ordinary differential equations (ODE) as an automatic control problem [16]. Subsequently, Gustafsson focused on stepsize control techniques for explicit and implicit Runge-Kutta methods [17,18]. Additional works expand on the topic and introduce the application of more advanced controllers and digital filters [19,20,21,22]. Another summary of numerical integration stepsize control may be found in Ref. 23.

A natural extension of numerical integration stepsize control is the control of the temporal discretization of data exchange between coupled physics. Valli and others have utilized proportional-integral-derivative (PID) controllers to select the time stepsize of the exchange of data between nonlinear iterations for coupled reaction-convection-diffusion and coupled viscous flow / heat transfer problems [24,25]. Stepsize control was achieved by monitoring normalized changes in solution variables of interest, such as velocity and temperature. More recently, a PI controller was parameterized for lattice physics depletion simulations [23]. Other interesting applications of adaptive stepsize control are found in Refs. 26 and 27.

3.2.1. Elementary Error Control

The introduction of stepsize control for numerical integration is best achieved by considering the ODE,

$$\frac{dy}{dt} = f(y), \qquad y(t_0) = y_0, \qquad t \geq t_0, \tag{10}$$

where the numerical solution at discrete time steps is sought. The stepsize h is used to advance the solution of the ODE from one state in time $y(t)$ to the next, $y(t + h)$, according to a prescribed error tolerance, ε. A popular elementary local error controller is given as

$$h_{n+1} = \left(\frac{\varepsilon}{\hat{r}_{n+1}}\right)^{\frac{1}{k}} h_n, \tag{11}$$

where k depends on the order of the method and $\hat{r}_{n+1}$ is the local error estimate [28]. The heuristic derivation of this control algorithm is given in Ref. 21; the important aspects are now summarized.

Consider the ODE in Equation 10 with a measure for the local error defined as $\hat{e}_{n+1} = y_{n+1} - \hat{y}_{n+1}$, where $\hat{y}_{n+1}$ is the discrete reference solution, which at the state $n+1$ has the same value as the continuous reference solution, $y(t_n + 1)$. The local error is assumed to depend on the stepsize asymptotically, $\hat{e}_{n+1} \sim h^{\hat{p}+1}$, where $\hat{p}$ is the order of the error estimate. Therefore, it is expanded in an asymptotic series as $\hat{e}_{n+1} = \widehat{\Phi}_n h^{\hat{p}+1} + O\left(h^{\hat{p}+2}\right)$, where $\widehat{\Phi}_n$ is the principal error function at state point n and is dependent on the ODE solution. The order of the error estimate, $\hat{p}$, is the largest integer for which $\hat{e}_{n+1} = O\left(h^{\hat{p}+1}\right)$ for all n. Depending on the control objectives, the local error is controlled by either the error per step (EPS) with $\hat{r}_{n+1} = \|\hat{e}_{n+1}\|$ and $k = \hat{p} + 1$, or by the error per unit step (EPUS) with $k = \hat{p}$ and

$$\hat{r}_{n+1} = \left\| \frac{\hat{e}_{n+1}}{h_n} \right\|. \tag{12}$$

The above derivation suggests that the difference between the tolerance, ε, and error estimate, $\hat{r}_{n+1}$, will be eliminated by the controller in a single step, thus decreasing the local error to the set tolerance. This ideal control is dependent on two assumptions. The first assumption is that the local error estimate varies asymptotically according to the relation

$$\hat{r}_{n+1} = \left\| \widehat{\Phi}_n \right\| h_n^k. \tag{13}$$

The second assumption is that the norm of the principal error function varies slowly,

$$\left\| \widehat{\Phi}_n \right\| = \left\| \widehat{\Phi}_{n-1} \right\|. \tag{14}$$

In practice, explicit calculation of the principal error function is not required.

3.2.2. Discrete-Time Integral Control

In this subsection, the interaction of the *process* and *controller*, known as *closed loop dynamics*, is developed. In the case of stepsize control of numerical integration, the process is the combination of the equation being solved and the integration method utilized. The controller is the means by which the error estimate and prescribed tolerance is used to control the stepsize.

The elementary error controller, Equation 11, is written as a linear difference (recurrence) equation by taking logarithms,

$$\log h_{n+1} = \log h_n + \frac{1}{k}(\log \varepsilon - \log \hat{r}_{n+1}). \tag{15}$$

The controller's objective is to seek an equilibrium where the control, $\log h_n$, of the current state n does not change in the next state $n+1$. This is achieved by forcing the error estimate, $\log \hat{r}_{n+1}$, equal to the setpoint, $\log \varepsilon$. The solution of Equation 15 is found as the sum of all past control errors,

$$\log h_n = \log h_0 + \frac{1}{k} \sum_{m=1}^{n} (\log \varepsilon - \log \hat{r}_m). \tag{16}$$

Assuming that the error evolves asymptotically according to Equation 13, taking the logarithm, eliminating the error estimate by combining with Equation 16, and replacing the $1/k$ factor with the integral gain, k_I , gives

$$\log h_{n+1} = (1 - kk_I) \log h_n + k_I\left(\log \varepsilon - \log\left\| \widehat{\Phi}_n \right\|\right). \tag{17}$$

The integral gain should be viewed as a design parameter (no longer fixed based on the process) with the purpose of affecting the closed loop dynamic behavior. The designer of the controller should determine proper gain values that produce good controller behavior. The root of Equation 17 is, $\lambda = 1 - kk_I$. Söderlind explains that the choice of kk_I is a tradeoff between the controller's response time and sensitivity to changes in $\log\|\widehat{\Phi}_n\|$. The I controller is given as

$$h_{n+1} = \left(\frac{\varepsilon}{\hat{r}_{n+1}}\right)^{k_I} h_n. \tag{18}$$

Comparison of the I controller to the elementary controller shows the singular difference is the substitution of $1/k$ for k_I, which results in smoother stepsize predictions, while still obeying the asymptotic error model given by Equation 13.The assumption of Equation 14 is no longer required.

Despite the I controller's smooth stepsize sequence, more advanced controllers may be used to improve performance and increase the range of applicability. The proportional-integral controller exhibits the benefits of integral control, but modifies the behavior with an additional proportional (P) action component. The PI controller includes two terms: (i) proportional to the control error, and (ii) proportional to the summation (discrete integral) of the control error. The PI controller may be derived in a similar fashion to the I controller; the final result is,

$$h_{n+1} = \left(\frac{\varepsilon}{\hat{r}_{n+1}}\right)^{k_I} \left(\frac{\hat{r}_n}{\hat{r}_{n+1}}\right)^{k_P} h_n. \tag{19}$$

The additional proportional component accounts for error trends and considers the local error estimate of the previous time step. Specifically, a quicker reduction of stepsize is achieved for increasing errors, and a quicker increase of stepsize is realized for decreasing errors. As with the I controller, the gains, k_I and k_P, associated with the PI controller should be determined based on the controller's objective and required behavior. Choosing k_I and k_P is a compromise between stability and response time.

3. METHOD

4.1. STAR-CCM+ Model

The fluid-dynamic simulation included conjugate heat transfer for the calculation of the temperature distribution in the fuel and cladding domains. A volumetric heat generation source was used in the fuel domain. The CFD domain includes the solid structure constituting the fuel pellet and cladding, the water domain in the subchannel surrounding the fuel pin, and three spacer grids with mixing vanes as shown in Figure 2 (right). Only the spacer grids where the highest fuel and cladding temperatures are expected are modeled; the other grids were not modeled to reduce computation time. The spacer grid regions, which rest at 203.28 cm, 249.00 cm, and 294.72 cm from the bottom of the active fuel, were discretized using polyhedral cells together with three layers of prismatic cells at the wall, as shown in Figure 2 (left). The computational mesh upstream and downstream of grid spacers was generated by extrusion, applying the hyperbolic tangent law. Approximately 1.6 million cells makeup this model.

The realizable k-ε turbulence model was first considered, but then abandoned due to numerical instabilities that persisted in regions away from the spacer grids where flow was predominantly in the axial direction. Sensitivity studies using various turbulence models and meshes were previously performed [29], and it was concluded that, for the integral parameters of interest, the two-equation RANS models give reasonable results. Moreover, according to a recent international benchmark, the k-ε model

shows good agreement with experimental data [30].

An inlet velocity of 5.278 m/s, inlet temperature of 556.76 K, and constant outlet pressure of 15.5 MPa were imposed as boundary conditions. Periodic boundary conditions were imposed on the lateral surfaces of the water domain (coolant subchannel). No-slip conditions were imposed on the spacer grids, pin walls and on the cladding surface. The coolant density was calculated according to the following third-order polynomial: $\rho(T) = -0.0000116905 \cdot T^3 + 0.01225 \cdot T^2 - 4.84697 \cdot T + 1670.325859$.

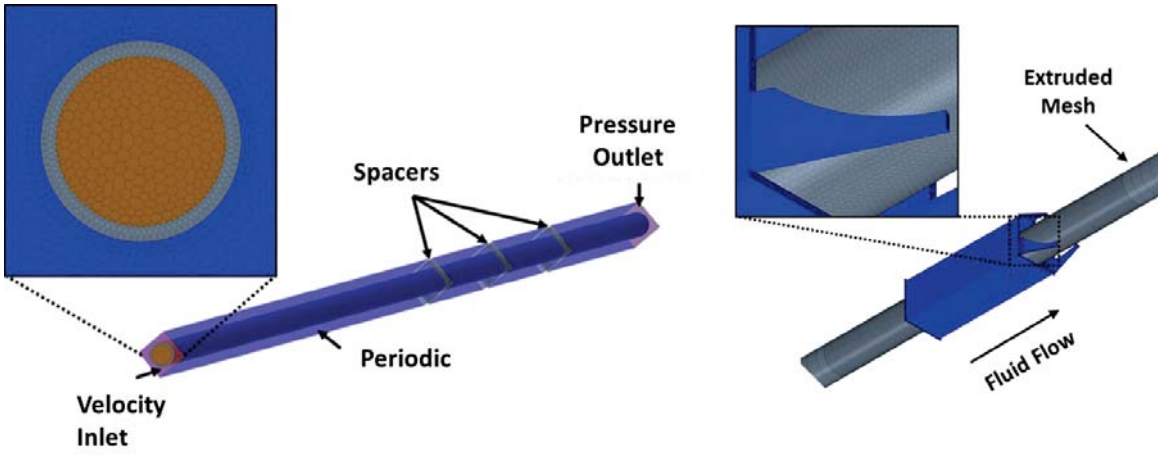

Figure 2. STAR-CCM+ single pin cell with three spacer grids polyhedral mesh model.

4.2. MAMBA Model

The 3-D CRUD deposition domain consists of a 365.76 cm long cladding surface with a radial mesh that *grows* in time in 5 μm increments as the CRUD deposit thickens. The circumferential, or azimuthal, discretization consists of 16 uniform sectors. The axial discretization is non-uniform and consists of planes with thicknesses ranging from 0.5 cm in the regions where CRUD deposition is expected to be the most aggressive (e.g. the top third of the fuel rod) to 4 cm in the rest of the domain (e.g. the lower two thirds).

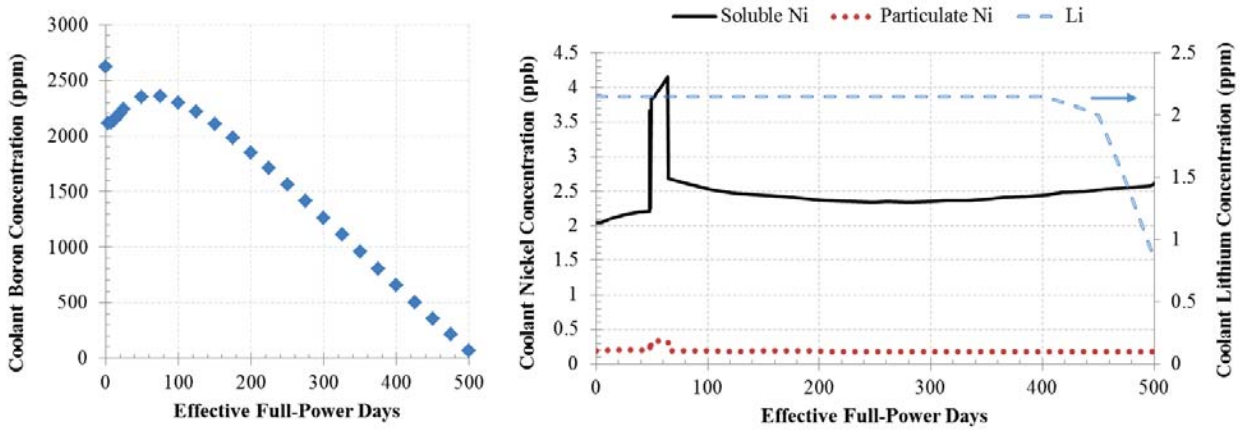

Figure 3. Coolant boron, nickel and lithium concentrations used in the CRUD deposition model.

In addition to the CRUD parameters defined in subsection 3.1, the dissolved boron, particulate nickel and soluble nickel concentrations within the coolant are functions of time as depicted in Figure 3. It is noted

that the coolant boron concentration curve predicted by the single pin cell DeCART model is much higher than typically used in a commercial PWR; this does impact the boron hideout prediction, but should not affect the conclusions drawn in this study.

4.3. Temporal Coupling

The loose coupling approach adopted between the thermal hydraulics and CRUD deposition physics removes the nonlinear dependence of the CRUD deposition process on the thermal hydraulic conditions of the plant. Subsequently, three temporal coupling methods are investigated, including a one-way coupling, a two-way lagged coupling, and a two-way predictor-corrector coupling. The one-way coupling, shown in Figure 4 (top-left), refers to a unidirectional data transfer from the CFD solver to the CRUD solver at the beginning of each time step. At each of these points in time, the CFD and neutronics solvers were iterated until convergence; therefore, the TH parameters at each step are computed based on a realistic power distribution as computed during cycle depletion. Figure 4 (top-right) illustrates a two-way coupling where the TH solution lags the CRUD deposition solution; a steady state CFD calculation is performed at the beginning of each coupled time step.

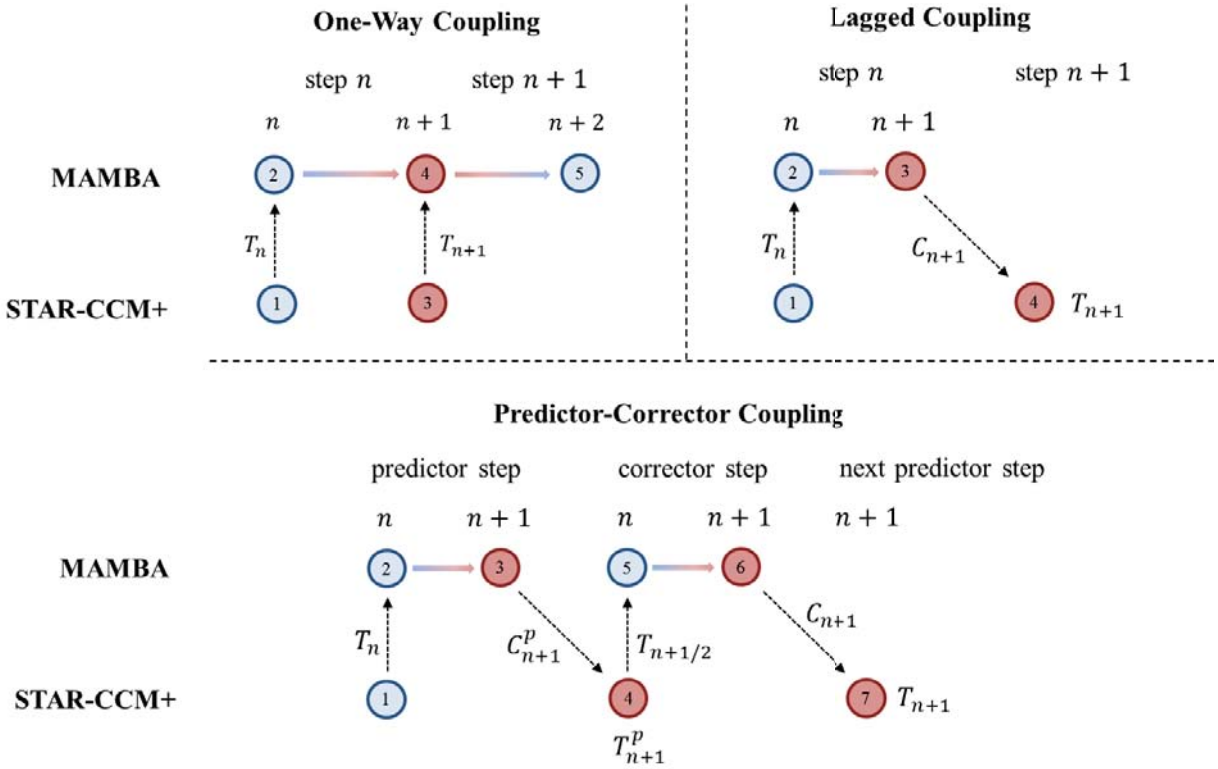

Figure 4. One-way (top-left), two-way time-lagged (top-right) and predictor-corrector (bottom) temporal coupling approaches compared for STAR-CCM+/MAMBA.

In the P-C coupling, the nonlinearity of the coupled solution is partially recovered, thus enabling a more accurate solution and often longer stepsizes in comparison to the explicit couplings. These benefits are realized at the cost of an additional solution of each of the physics during every time step, as depicted in Figure 4 (bottom). The P-C algorithm is outlined as:

a. calculate the beginning-of-step (BOS) TH properties, T_n, using the CRUD properties, C_n,

b. deposit CRUD with C_n to the EOS using T_n to obtain the predicted EOS CRUD inventory, C^p_{n+1},

c. calculate T_{n+1}^{p} using C_{n+1}^{p},

d. average the predictor and corrector TH properties to obtain the middle-of-step (MOS) TH data set, $T_{n+1/2} = \frac{1}{2}\left(T_n + T_{n+1}^{p}\right)$,

e. and, re-deposit C_n to EOS using $T_{n+1/2}^{p}$ to obtain C_{n+1}.

4.4. Stepsize Controller Parameterization

Extension of the predictor-corrector algorithm to enable a stepsize controller is straight forward. One additional step is added to the algorithm above, where the difference in the final CRUD state C_{n+1} and the predicted state C_{n+1}^{p} is calculated and used as a solution residual. The *error per unit step* method is employed as given by Equation 12, where stepsizes are calculated in days. The relative error in the integral boron mass (for the entire fuel rod) is used to calculate the convergence residual $\|\hat{e}_{n+1}\|$,

$$\|\hat{e}_{n+1}\| = \frac{\left|C_{n+1} - C_{n+1}^{p}\right|}{C_{n+1}}. \tag{21}$$

Both I and PI controllers were investigated for controlling the coupled CRUD deposition solution. Parameterizing the controllers involved determining an acceptable tolerance on the boron mass solution and appropriate gain values to result in overall good dynamic behavior. First, an I controller was considered and the integral gain was varied between 0.05 and 0.3 in combination with varying the boron mass tolerance between $1x10^{-3}$ and $1x10^{-6}$. Increasing the integral action results in a slower response to changes in the error, e.g. if the error increases, the stepsize reduction is slow, or may appear delayed. Reasonable stepsize predictions were achieved with integral gains around 0.1 and a boron mass tolerance around $1x10^{-4}$.

Next, the addition of a proportional error component was considered. The proportional gain was varied between 0.05 and 0.4 in combination with the integral gain and boron concentration tolerances previously mentioned. Generally, increasing the proportional action results in a quicker response to changes in the error, which may offset the slow response of the integral action; thus, a balance of the integral and proportional action is sought. However, if the transient response is too high (too large proportional gain), oscillatory behavior in the stepsize adjustments may be encountered.

Based on the parameter testing described above, a boron mass tolerance of $1x10^{-4}$ is recommended in combination with a PI controller with an integral gain of 0.05 and a proportional gain of 0.1. It is noted that proportional gains above 0.2 induce stepsize oscillations as the feedback dynamics is too sensitive and responds too quickly. Also, decreasing the integral gain results in smoother, damped stepsize sequences, which usually means increasing the overall number of time steps within the cycle. The parameterization given above provides a good balance and gives acceptable behavior for the classes of problems tested. To begin the cycle, the initial time stepsize is fixed at 25 days until boron appears within the CRUD deposit. Then, an I controller is used for the first time step where boron may be monitored because higher-order controllers, such as PI, require additional information to be known. Each predicted stepsize is rounded to the nearest 5 days.

4. RESULTS

4.1. Fixed Stepsize Sequence

The temporal coupling of steady state thermal hydraulics, via computational fluid dynamics (CFD), and time-dependent CRUD deposition has been investigated for a 500-day operating cycle. In this section, the

results of three fixed stepsize methods are reported. Precomputed power density distributions were supplied (by the neutronics code DeCART) to the CFD solver at each time step for all cases compared.

Figure 5 shows the boron hideout mass for the various temporal discretizations and coupling methods. The point in time at which the boron precipitation begins is unknown *a priori* and is dependent on several coupled factors, including temperature, heat flux, and species concentration. Prior to 125 days, the predicted boron hideout mass is relatively insensitive to the coupled temporal discretization; however, as the precipitation threshold for the lithium tetraborate reaction (Equation 5) is reached within the CRUD chemistry solver, the solution sensitivity to the TH boundary conditions increases substantially. Moreover, depending on the temporal discretization, the point at which the boron mass reaches a maximum varies due to the neutronics coolant boron concentration condition. As the critical boron concentration required to maintain criticality decreases throughout the cycle, the precipitation of solid boron species slows and eventually stops. Subsequently, the integral boron mass decreases, as shown in the comparison in Figure 5 (top-left), due to boron species diffusion within the CRUD layer.

Figure 5 (top-left) also shows the strong effect the coupled stepsize, or frequency of updating the thermal hydraulic boundary conditions within the CRUD solver, has on the boron mass prediction for a one-way coupling, i.e. no feedback through the CFD solver. At the end-of-cycle (EOC), the boron mass is over-predicted by 50% for the 50-day simulations when compared to the P-C reference 5-day case. Similarly, the fixed 25-day and 5-day one-way coupled approaches over predict the boron mass by 23%.

Figure 5 (middle-left) shows the boron mass predictions for the two-way coupling cases, where the thermal hydraulic solution lags the CRUD deposition. In general, introducing the thermal hydraulic boundary condition updates results in less boron mass within the CRUD deposit, especially for larger time stepsizes. This is primarily due to the heat flux distribution, resulting for the power density distribution that changes during depletion. Clearly, a fixed stepsize of 50 days is too large; whereas, the 5-day solution differs by less than 10% from the reference.

Figure 5 (bottom-left) compares the predictor-corrector coupling approach for the fixed stepsizes of 50, 25, and 5 days. A significant improvement in the coarse 50-day solution is noted when using this method. The largest differences from the reference occur around the point in time where boron begins to precipitate, and the CRUD chemistry conditions are most sensitive to the thermal hydraulic state. The 25-day case captures this region in time better, but under predicts the boron mass even more so than the 50-day case by the end of the cycle. This is likely due to nonlinear (in time) variations in the heat flux distribution, so when the predictor and corrector TH parameters are averaged within the time step, the boron mass prediction may increase or decrease with stepsize refinement.

Figure 5 (right column) compares boron mass predictions for the various temporal coupling approaches for the 50 day fixed stepsize (top-right), 25 day fixed stepsize (middle-right), and the 5 day fixed stepsize (bottom-right). As previously mentioned, the P-C method with a fixed stepsize of 50 days actually performs quite well; the additional computations necessary for the method are rewarded with a fewer number of time steps as well as increased accuracy.

Figure 5 (middle-right and bottom-right) compares the coupling methods for the 25 and 5 day stepsize lengths, respectively. The one-way and two-way lagged methods consistently over-predict the boron mass, which is likely due to the heat flux and cladding temperature are typically decreasing in time (with depletion), so lagging the TH boundary condition updates on the CRUD solution results in higher boundary condition values and thus more boron mass. On the other hand, the 25-day P-C method consistently under predicts the EOC boron mass; similarly, this is due to the P-C method linearly interpolating the nonlinear coupled solution.

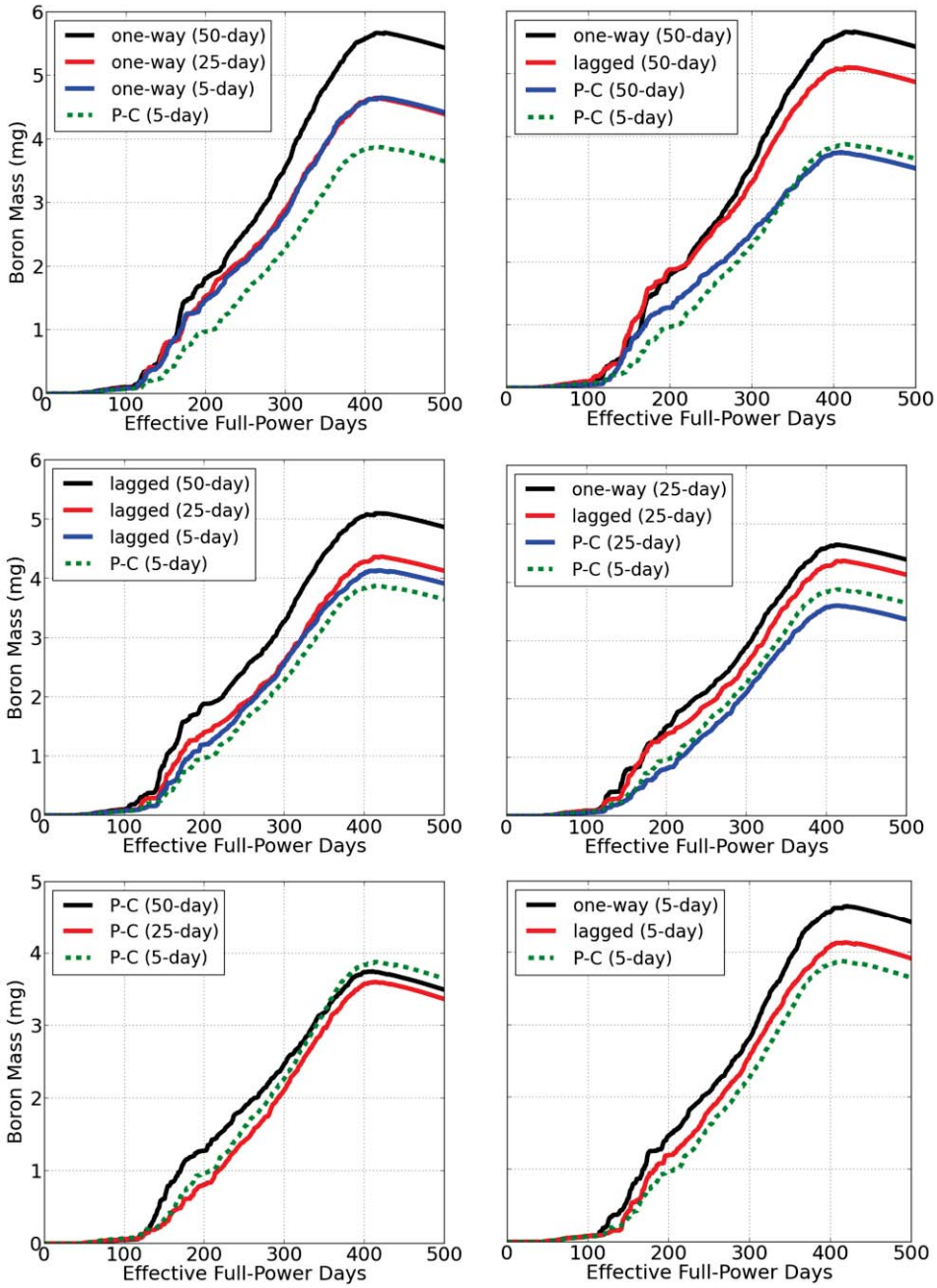

Figure 5. Boron mass prediction for one-way (top-left), two-way lagged (middle-left), and P-C (bottom-left) couplings using 50, 25, and 5 day fixed time stepsizes. Comparison of boron mass prediction for the three temporal coupling approaches for 50 day stepsizes (top-right), 25 day stepsizes (middle-right), and 5 day stepsizes (bottom-right) to the reference 5 day P-C solution.

5.2. Adaptive Stepsize Selection

The adaptive stepsize controller predictions for the stepsize (left) and boron mass (right) are compared with the 5 day P-C reference case in Figure 6. The boron mass prediction is reasonable with a relative error of about 5% at the end of the cycle. The number of time steps has been reduced from 20 steps for the 25 day fixed stepsize case to 18 steps in the adaptive case. Additionally, a small gain in accuracy of approximately 1-2% is realized.

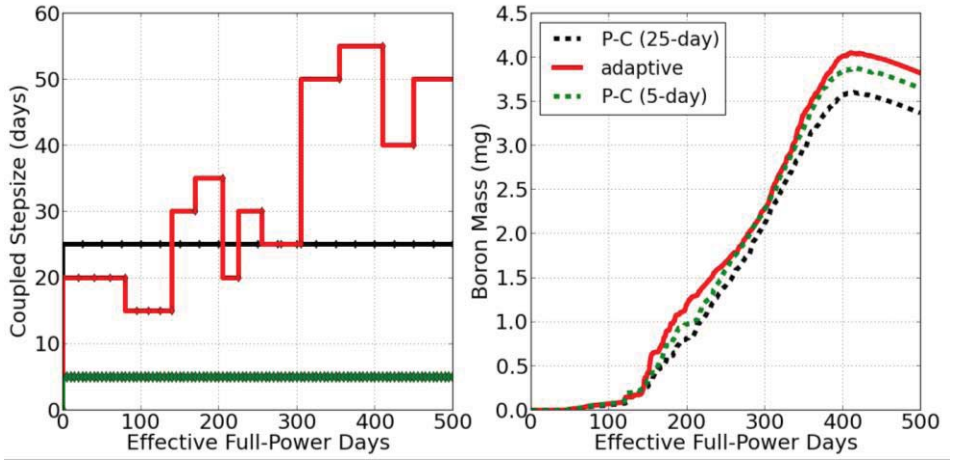

Figure 6. Stepsize (left) and boron mass (right) comparison of adaptive and reference solutions.

5. CONCLUSIONS

The temporal coupling of the CFD and CRUD deposition physics was investigated for a single fuel pin cell with spacer grids and mixing vanes under typical PWR operating conditions. An adaptive stepsize selection algorithm based on control theory was developed. Monitoring the changes in the total boron concentration between predictor and corrector calculations allowed control of the convergence residual of the thermal hydraulic and CRUD deposition calculations. A proportional-integral, PI, controller was implemented and parameterized. A boron mass tolerance of $1x10^{-4}$, integral gain of 0.05, and proportional gain of 0.1 is recommended.

Despite considerably reducing the coupled stepsize to 5 days for the one-way method, the boron mass error is more than 20% at the end of the cycle. Similarly, the lagged two-way boron mass prediction with 5-day stepsizes is over predicted by more than 7%. On the other hand, the predictor-corrector method allows coarse stepsizes on the order of 50 days with comparable or better accuracy when compared to all other methods and stepsizes, other than the 25-day P-C case. Extending the P-C method to an adaptive stepsize selection method shows promise by reducing the number of time steps taken and increasing the accuracy when compared to the fixed step methods. Using the controller parameterization defined above, the average predicted stepsize is about 25 days. Further optimization of the stepsize controller may be possible, thus additional parmaterizations and the addition of derivative action should be considered.

ACKNOWLEDGMENTS

This work was partially supported by the NRC faculty development grant NRC-HQ-11-G-38-0038 and by a DOE NEUP grant.

REFERENCES

1. D. Walter, et al., "High-fidelity simulation of crud deposition on a fuel pin with grid spacers - a proof-of-principle using the fully coupled MAMBA/DeCART/STAR-CCM+ code", *Proc. of NURETH-15*, Pisa, Italy, May 12-16 (2013).
2. V. Petrov, et al., "Impact of fluid-dynamic 3D spatial effects on the prediction of crud deposition in a 4x4 PWR sub-assembly", *Proc. of NURETH-15*, Pisa, Italy, May 12 - 16 (2013).
3. V. Petrov, et-al., "Prediction of CRUD deposition on PWR fuel using a state-of-the-art CFD-based multi-physics computational tool," *Proc. Of CFD4NRS-5*, Zurich, Switzerland, September 9-11 (2014). Selected for a special issue of *Nuclear Engineering and Design.*

4. J. Secker, "Coupled ANC/VIPRE/BOA multi-physics results for Watts Bar I cycles 1-3", CASL report CASL-2011-0125-000-CI, L1:CASL:P2:03.
5. J. Secker, "Coupled ANC/VIPRE/BOA multi-physics standard and fine mesh models for Vogtle I cycles 12-14", CASL report CASL-CI-2012-0091-000, L3:AMA:CHLNG:P4.01.
6. CD-adapco, "USER GUIDE STAR-CCM+ Version 8.02.008", (2013).
7. J. Deshon, et al., "PWR Fuel Crud and Corrosion Modeling", Advanced Fuel Performance: Modeling and Simulation, *JOM,* **63**(8) (2011).
8. M. Hursin, et al., "DeCART v2.05 Theory Manual", University of Michigan (2008).
9. W. Byers, W. Lindsay, R. Kunig, "Solubility of Lithium Monoborate in High-Temperature Water", *Journal of Solution Chemistry,* **29**(6), pp. 541-559 (2000).
10. B.K. Kendrick, J. Barber, "Initial validation and benchmark study of 3D MAMBA v2.0 against the WALT loop experiment and BOA v3.0". *CASL report MPOCRUD.P5.02*, 2012.
11. S.E. Ziemniak, et al., "Immiscibility in the nickel ferrite-zinc ferrite spinel binary", *Journal of Physics and Chemistry of Solids,* **68**, pp. 1476-1490 (2007).
12. P. Cohen, "Heat and mass transfer for boiling in porous deposits with chimneys". *AIChE Symposium Series*, **70**(138), (1974).
13. J. Henshaw, et al., "A model of chemistry and thermal hydraulics in PWR fuel crud deposits", *Journal of Nuclear Materials,* **353**, pp. 1-11 (2006).
14. EPRI, "Boron-Induced Offset Anomaly (BOA) Risk Assessment Tool", Report #1003211, Version 1.0, Palo Alto, CA (2003).
15. J. Deshon, et al., "Simulated Fuel Conductivity Measurements under Pressurized Water Reactor Conditions", Technical Report #1022896, EPRI, Palo Alto, CA (2011).
16. K. Gustafsson, M. Lundh, G. Söderlind, "A PI stepsize control for the numerical solution for ordinary differential equations", *BIT*, **28**, pp. 270-287 (1988).
17. K. Gustafsson, "Control theoretic techniques for stepsize selection in explicit Runge-Kutta methods", *ACM Transactions in Mathematical Software*, **17**, pp. 533-554 (1991).
18. K. Gustafsson, "Control theoretic techniques for stepsize selection in implicit Runge-Kutta methods", *ACM Transactions in Mathematical Software,* **20**, pp. 496-517 (1994).
19. K. Gustafsson, G. Söderlind, "Control Strategies for the Iterative Solution of Nonlinear Equations in ODE Solvers", *SIAM J. Sci. Comput*, **18**, pp. 23-40 (1997).
20. G. Söderlind, "The Automatic Control of Numerical Integration", *DWI Quart*, **11**, pp. 55-74 (1998).
21. G. Söderlind, "Automatic control and adaptive time-stepping*", Num. Alg.*, **31**, pp. 281-310 (2002).
22. G. Söderlind, "Digital Filters in Adaptive Time-Stepping", *ACM Trans. Math. Software*, **29**, pp. 1-26 (2003).
23. D. Walter, A. Manera, "A Control Theory Approach to Adaptive Stepsize Selection for Lattice Depletion Simulations", *Proc. of M&C*, Nashville, TN, April 19-23 (2015).
24. A.M.P. Valli, G.F. Carey, A.L.G.A. Coutinho, "Control strategies for timestep selection in simulation of coupled viscous flow and heat transfer", *Comm. in Num. Methods in Eng.*, **18**, pp. 131-139 (2002).
25. A.M.P. Valli, G.F. Carey, A.L.G.A. Coutinho, "Control strategies for timestep selection in finite element simulation of incompressible flows and coupled reaction-convection-diffusion processes", *International Journal for Numerical Methods in Fluids*, **47**, pp. 201-231 (2005).
26. P.M. Burrage, R. Herdiana, K. Burrage, "Adaptive stepsize based on control theory for stochastic differential equations", *Journ. of Comp. and App. Math.*, **170**, pp. 317-336 (2004).
27. J. Geiser, C. Fleck, "Adaptive Step-Size Control in Simulation of Diffusive CVD Processes", *Mathematical Problems in Engineering*, **2009**, pp. 1-34 (2009).
28. E. Hairer, *Solving Ordinary Differential Equations I*, Springer-Verlag (1993).
29. B.K. Kendrick, et al., "CILC Studies with Comparative Analysis to Existing Plants", *CASL report L2.MPO.P7.06* (2013).
30. Nuclear Energy Agency, "Report of the OECD/NEA KAERI Rod Bundle CFD Benchmark Exercise", NEA/CSNI/R(2013)5.